JGR Solid Earth

RESEARCH ARTICLE
10.1029/2022JB025168

Double-Difference Adjoint Tomography of the Crust and Uppermost Mantle Beneath Alaska

Guoxu Chen[1,2], Jing Chen[2], Carl Tape[3], Hao Wu[1], and Ping Tong[2,4,5]

[1]Department of Mathematical Sciences, Tsinghua University, Beijing, China, [2]School of Physical and Mathematical Sciences, Nanyang Technological University, Singapore, Singapore, [3]Geophysical Institute and Department of Geosciences, University of Alaska, Fairbanks, AK, USA, [4]Asian School of the Environment, Nanyang Technological University, Singapore, Singapore, [5]Earth Observatory of Singapore, Nanyang Technological University, Singapore, Singapore

Guoxu Chen and Jing Chen contributed equally to this work.

Key Points:

- Double-difference adjoint waveform tomography is applied to image the P-wave velocity structure of the crust and uppermost mantle of Alaska
- The imaged high-velocity mantle wedge under the Denali Volcanic Gap suggests minimal melt accumulation
- A slab gap is resolved beneath the Wrangell Volcanic Field

Supporting Information:

Supporting Information may be found in the online version of this article.

Correspondence to:

P. Tong,
tongping@ntu.edu.sg

Citation:

Chen, G., Chen, J., Tape, C., Wu, H., & Tong, P. (2023). Double-difference adjoint tomography of the crust and uppermost mantle beneath Alaska. *Journal of Geophysical Research: Solid Earth*, *128*, e2022JB025168. https://doi.org/10.1029/2022JB025168

Received 13 JUL 2022
Accepted 23 DEC 2022

Author Contributions:

Conceptualization: Ping Tong
Data curation: Guoxu Chen
Funding acquisition: Hao Wu, Ping Tong
Investigation: Guoxu Chen, Carl Tape
Methodology: Guoxu Chen, Jing Chen, Hao Wu, Ping Tong
Project Administration: Ping Tong
Resources: Hao Wu
Software: Guoxu Chen, Jing Chen, Carl Tape
Supervision: Carl Tape, Hao Wu, Ping Tong
Validation: Guoxu Chen, Jing Chen
Visualization: Guoxu Chen, Jing Chen
Writing – original draft: Guoxu Chen
Writing – review & editing: Guoxu Chen, Jing Chen, Carl Tape, Hao Wu, Ping Tong

Abstract We perform adjoint waveform tomography to reveal the P-wave velocity structure of the crust and uppermost mantle in Alaska by using common-source double-difference traveltime data. Our underlying forward modeling tool is a 3D seismic-wave solver called SPECFEM3D_GLOBE. We select ∼13,000 high-quality P-wave arrivals from 147 earthquakes recorded by more than 600 stations. The waveforms are filtered between 15 and 8 s and used to generate about 100,000 differential traveltimes via the cross-correlation technique. We invert these common-source differential traveltimes for a P-wave velocity model down to 150 km depth in Alaska. In the upper mantle, a high-velocity zone is imaged along the Aleutian volcanic arc, which represents the Pacific plate subducting beneath the North America plate. On the eastern edge of the subducting Pacific plate, the imaged high-velocity anomaly extends distinctly beyond the Wadati–Benioff zone, indicating an aseismic slab edge. We observe an absence of a low-velocity mantle wedge beneath the Denali Volcanic Gap (DVG) in our tomographic model. This finding suggests that minimal melt accumulation exists beneath the DVG, which may explain the cessation of magmatism there. Our model also reveals a high-velocity anomaly near the Wrangell Volcanic Field (WVF), suggesting the possible existence of the Wrangell slab or the high-velocity slab edge of the Yakutat slab. A potential slab gap shown as a low-velocity body is detected at 95–125 km depth near the WVF, which could act as a channel to transport mantle materials to feed the cluster of volcanoes in the WVF.

Plain Language Summary Characterizing the subsurface structure of Earth's interior is achieved by recording how seismic waves—originating from earthquakes—travel different speeds depending on the materials through which they travel. We focus on using the traveltimes of seismic waves from earthquakes in Alaska to produce a tomographic image of the subsurface variations of Alaska. Our technique differs from previous approaches in that we rely on differences in traveltimes from earthquakes to stations that are close to each other, which can be calculated by correlating the shapes of recorded waveforms. Our resulting tomographic image reveals major plate tectonic features, such as the subducting Pacific plate and volcanic regions. Our technique and resulting images enable a better understanding and interpretation of the subsurface structure and geodynamics of Alaska.

1. Introduction

Alaska is one of the most seismically active areas in the world. It is composed of various terranes accreted from different geologic times (Colpron et al., 2007; Plafker & Berg, 1994) and exhibits distinctive and complicated geological environments. Along the Aleutian-Alaska subduction zone, the Pacific plate subducts beneath the North America plate at a rate of approximately 5 cm/year (DeMets et al., 1994) (Figure 1a), producing abundant seismicity and arc volcanism. At the eastern edge of the subducting Pacific plate, the Yakutat terrane, a thick and buoyant oceanic plateau (Mann et al., 2022), has partially subducted beneath Alaska at a shallow angle (Benowitz et al., 2014; Christeson et al., 2010; Eberhart-Phillips et al., 2006; Ferris et al., 2003). The shallowing of the slab dip angle may be responsible for the cessation of magmatism beneath the Denali Volcanic Gap (DVG) (Martin-Short et al., 2018) and associated with the clustering of volcanoes in the Wrangell Volcanic Field (WVF). These distinct features make Alaska a natural laboratory to investigate subduction processes and the origins of magmatism.

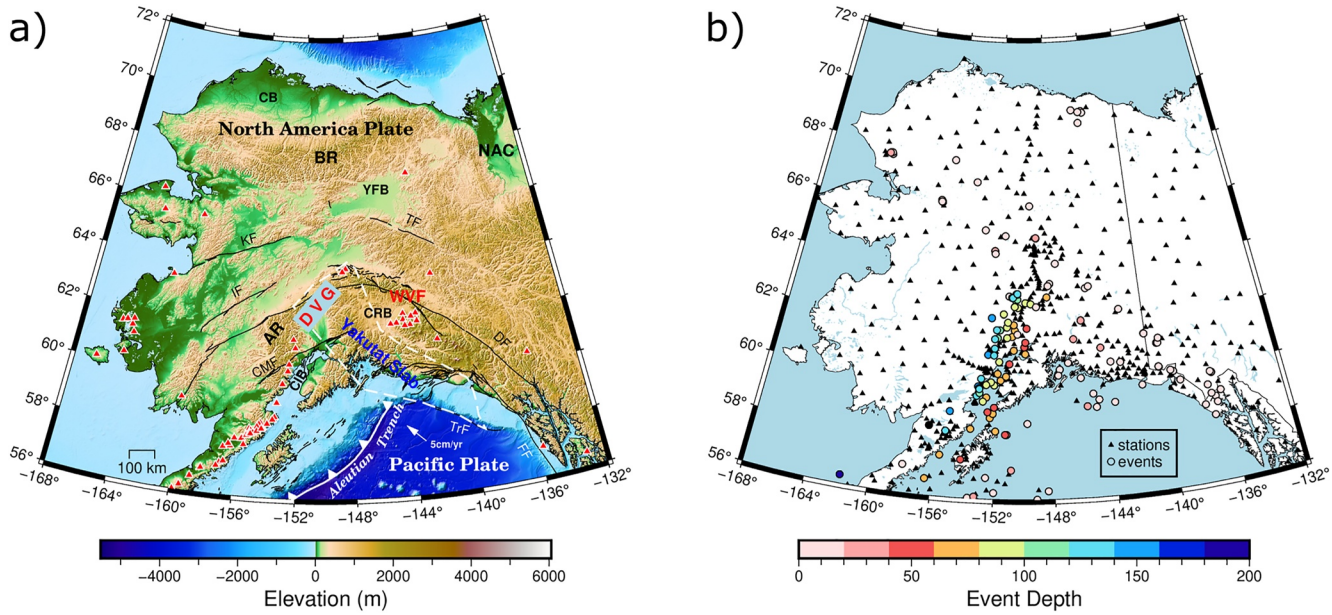

Figure 1. (a) Tectonic setting in Alaska. The black solid lines denote the Quaternary faults and folds of Alaska provided by the United States Geological Survey (https://www.usgs.gov/natural-hazards/earthquake-hazards/faults). The red triangles show active volcanoes in the last 2 Myr (Cameron, 2004). The subducted Yakutat slab is outlined by white dashed lines (Eberhart-Phillips et al., 2006). Tectonic features are labeled as: TF, Tintina fault; KF, Kaltag fault; IF, Iditarod-Nixon Fork fault; DF, Denali fault; CMF, Castle Mountain fault; TrF, Transition fault; FF, Fairweather fault; NAC, North American craton; BR, Brooks Range; AR, Alaska Range; CB, Colville basin; YFB, Yukon Flats basin; CIB, Cook Inlet basin; CRB, Copper River basin; DVG, Denali Volcanic Gap; WVF, Wrangell Volcanic Field. (b) Earthquakes (dots color-coded by depth) and stations (black triangles) used in this study.

Crustal and upper mantle structures beneath Alaska have been examined by previous seismic imaging studies using various seismic data and tomography methods, for example, body wave traveltime tomography (Eberhart-Phillips et al., 2006; Kissling & Lahr, 1991; Qi et al., 2007; Tian & Zhao, 2012; Zhao et al., 1995), receiver function analysis (Ferris et al., 2003), surface wave tomography (Wang & Tape, 2014), and ambient noise tomography (Ward, 2015).

By 2017, the EarthScope USArray Transportable Array (TA) was fully deployed in Alaska, providing new station coverage in western Alaska, northern Alaska, and northwestern Canada (Busby & Aderhold, 2020). This network, together with other permanent and temporary networks, ushered in a new era of monitoring and seismic imaging in Alaska (e.g., Berg et al., 2020; Feng & Ritzwoller, 2019; Gou et al., 2019; Jiang et al., 2018; Martin-Short et al., 2018; Miller & Moresi, 2018; Nayak et al., 2020; Ward & Lin, 2018; Zhang et al., 2019, and others). Jiang et al. (2018) imaged the S-wave velocity structure down to 800 km depth in Alaska by combining Rayleigh wave dispersion measurements with teleseismic S-wave traveltime data. Their findings demonstrated that the Yakutat slab extends further to the northeast than previous studies suggested. In addition, a high Vs anomaly was revealed beneath the WVF and interpreted as a potential slab fragment that contributes to the Wrangell magmatism. Using regional and teleseismic P-wave arrival times, Gou et al. (2019) established a refined anisotropic P-wave velocity model which shows that the Pacific plate has subducted down to 450–500 km depth below central Alaska. They also reported a slab gap at 65–120 km depth beneath the WVF, which is possibly the magma channel through which mantle materials are transported upward to feed volcanoes. Using body-wave traveltimes and ambient-noise-derived surface-wave data, Nayak et al. (2020) presented the Vp and Vp/Vs ratio models of Alaska. The models show a distinct high-velocity anomaly at ~65 km depth below the DVG, suggesting no partial melting in the mantle wedge.

These new tomographic models exhibit differences that pose challenges toward understanding magmatism and volcanism in Alaska. In south-central Alaska, the Denali Volcanic Gap (DVG) separates the subduction-induced volcanic arc into two parts: the Aleutian volcanic arc and the Buzzard Creek–Jumbo Dome (BC-JD) volcanoes (Figure 1a). The cause of this unusual volcanic gap is still unclear. The different patterns of Wadati-Benioff zone seismicity beneath the DVG and the Pacific plate likely reflect the different dehydration states of the Yakutat crust and the Pacific crust (Chuang et al., 2017; Martin-Short et al., 2018). One hypothesis for the DVG, proposed

by McNamara and Pasyanos (2002), is that melted material cannot reach the surface. In their results, derived from regional Pn and Sn traveltimes, a low-velocity and high Poisson's ratio uppermost mantle is imaged beneath the DVG. This anomaly is similar to what exists beneath the volcanoes, indicating the mantle wedge beneath the DVG is similar in composition and thermal properties despite the absence of volcanic activities on the surface. In contrast, some recent studies have suggested the depletion of melt beneath the DVG (Berg et al., 2020; Chuang et al., 2017; Jiang et al., 2018; Nayak et al., 2020; Yang & Gao, 2020).

Another open topic is the evolution of volcanism in the WVF. Some tomographic models have imaged a high-velocity anomaly in the mantle beneath the WVF, suggesting a possible slab tear in this area, as a magma channel to feed Wrangell volcanoes (Gou et al., 2019; Jiang et al., 2018; Yang & Gao, 2020). Other investigations (Berg et al., 2020; Martin-Short et al., 2018) did not find high-velocity anomalies representing the Wrangell slab beneath the WVF, and they reported that the volcanism in the WVF is partially attributed by the melting of the Yakutat slab.

In this paper, we apply the adjoint waveform tomography method (Yuan et al., 2016) using common-source double-difference traveltime data to reveal the P-wave velocity structure of the crust and uppermost mantle beneath Alaska. This method involves two key components: solving the elastic wave equation and using robust double-difference traveltime data. First, we solve elastic wave equations using 3D wavefield simulations, which provide synthetic waveforms for comparison with observed waveforms. The wave equation-based modeling method naturally incorporates the finite-frequency effects of wave propagation such as wavefront healing and scattering (Dahlen et al., 2000; Hung et al., 2001), which enhances the resolvability of small anomalies (Liu & Tromp, 2006; Pratt, 1999). Second, unlike traditional inversion methods to minimize the mismatch between synthetic signals and observed signals, we measure the double-difference traveltimes

$$\Delta\Delta t = \Delta t_{obs} - \Delta t_{syn}, \tag{1}$$

where

$$\Delta t_{obs} = \arg\max_{\tau} \int_0^T d_1^{obs}(t+\tau) d_2^{obs}(t) \mathrm{d}t, \tag{2}$$

is the cross-correlation traveltime difference of observed waveforms recorded by two seismic stations and, replacing "obs" with "syn," Δt_{syn} is the cross-correlation traveltime difference of synthetic waveforms computed in a 1D or 3D Earth model. With these measurements, several uncertainties can be accounted for, including within the assumed source-time function, the origin time, and recorded signal amplitudes. Furthermore, these measurements can reduce the effects of uneven event distribution (Yuan et al., 2016). As a result, the adjoint waveform tomography method using common-source double-difference traveltime data offers an effective and reliable approach for subsurface imaging. Yuan et al. (2016) provided a convincing synthetic test to illustrate the higher resolution of the double-difference method compared to the conventional wave equation-based traveltime tomography method, and Chen et al. (2022) demonstrated a successful application to northeast Japan. Here we apply this new method to Alaska.

The paper is organized as follows. In Section 2, we introduce the seismic stations and earthquakes used in the inversion, as well as the procedures to process waveform data. Then we discuss the forward wavefield simulation, the initial model, and the inversion method in Section 3. Section 4 contains the inversion results derived from real seismic data and the results of checkerboard and restoring resolution tests. In Section 5, we discuss the imaged velocity anomalies.

2. Data

2.1. Seismic Stations and Earthquakes

Our study area includes mainland Alaska and part of the Aleutian volcanic arc, with latitude ranging from 56° to 72° and longitude ranging from −168° to −132°. The regional earthquake catalog is collected from the Advanced National Seismic System Comprehensive Earthquake Catalog (ANSS ComCat) of the United States Geological Survey. Vertical-component seismic waveforms are downloaded from the Incorporated Research Institutions for Seismology Data Management Center (IRIS DMC).

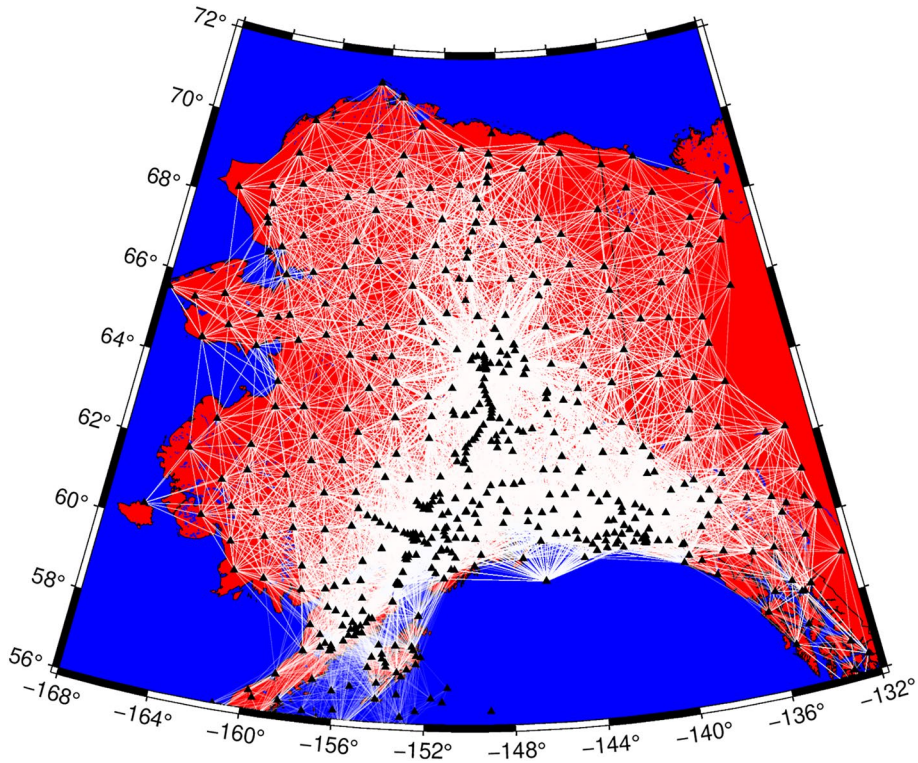

Figure 2. Station pairs used in our tomographic inversion. Each pair of stations with a measured differential traveltime is connected with a white line.

The computational cost of adjoint-based imaging approaches generally scales with the number of earthquakes (or, in the case of ambient noise adjoint tomography, the number of stations). To balance data coverage and computational cost, we carefully choose 147 earthquakes occurring from 2000 to 2021 with magnitudes ranging from 3.1 to 7.9 (Figure 1b). The number of used earthquakes per year is displayed in Figure S1 of Supporting Information S1. Each selected earthquake contributes more than 100 reliable differential traveltimes, providing dense data coverage in southern and central Alaska (Figure 2).

Differential traveltimes are measured on more than 600 seismic stations (mostly broadband seismographs) from 29 networks (Table S1 in Supporting Information S1). More than half of the total are from the Transportable Array (160; network TA) and Alaska Regional Network (190; network AK). Station spacing is approximately 85 km apart in the study region (Figure 1b). There are other temporary or permanent seismic networks (e.g., networks AV, XE, XZ, YM, ZE), providing denser station coverage in south-central Alaska. Waveform data from the recently deployed network AACSE (Alaska Amphibious Community Seismic Experiment; network XO) are also used, enhancing the coverage around the Alaska Peninsula.

2.2. Waveform Data Processing

To reliably measure the traveltime difference between two waves emanating from the same earthquake but arriving at two neighboring stations, we take five steps to preprocess raw waveform data:

1. Remove the instrument response, the mean, and the linear trend from the raw seismograms to retrieve ground displacement.
2. Filter the waveforms using a second-order Butterworth band-pass filter with corner frequencies of 0.067 Hz (15 s) and 0.125 Hz (8 s).
3. Resample waveforms to 100 Hz, which enables a minimum calculated cross-correlation traveltime difference of 0.01 s.
4. Choose an appropriate time window that contains the first P waves for measuring the traveltime difference. The waveform time window in this study is designed to be from 15 s before to 15 s after the first P-wave arrival

time. Note that the first P-wave arrival times are downloaded from the Alaska Earthquake Center (AEC) and the National Earthquake Information Center of the United States Geological Survey (USGS), or theoretically predicted by using the software package TauP (Crotwell et al., 1999) based on the AK135 reference model (Kennett et al., 1995) if not recorded by these two centers.

5. Exclude waveforms on the basis of low signal-to-noise ratios (SNR). Here signal energy is the L^2 norm of the signal from 5 s before to 15 s after the first P arrival time; the noise energy is from 15 to 5 s before the P arrival. We retain signals having SNR greater than 8.

After preprocessing the waveform data, we calculate the traveltime difference of two waves from the same earthquake but recorded by two separate stations via the cross-correlation technique. Three selection criteria are applied to obtain reliable differential traveltimes for each iteration.

1. The cross-correlation coefficient for two waveforms must be at least 0.8 in order for the differential traveltime measurement to be kept.
2. The difference of the azimuthal angles measured at two compared seismic stations should be smaller than 30°. This requirement ensures similar wave propagation paths so that the uncertainty of source-side structure is reduced.
3. The maximum inter-station distance is set as 300 km, which is comparable to the width of the first Fresnel zone (Baig et al., 2003; Woodward, 1992; Yuan et al., 2016).

Figure 3 shows an example of selecting differential traveltimes for observed waveforms. We also want to declare that in each iteration, only station pairs with double-difference traveltime less than 2 s (i.e., $|\Delta t_{obs} - \Delta t_{syn}| \leq 2$ s) will be used considering the reliability of the data. Applying our selection criteria to the set of 147 earthquakes, we measured 105,544 differential traveltimes from 13,202 first P-wave arrivals, yielding dense data coverage throughout Alaska, particularly in central and southern areas (Figure 2).

3. Method

3.1. Wavefield Simulations

We use the software package SPECFEM3D_GLOBE (Komatitsch & Tromp, 2002a, 2002b; Liu & Tromp, 2008; Peter et al., 2011) to simulate seismic wave propagation and calculate sensitivity kernels. This package employs the spectral element method to solve the wave equation, and it is suitable for complex geometries. It also achieves high numerical accuracy (Komatitsch & Vilotte, 1998) and is readily implemented for parallel computing (Komatitsch, 2011; Komatitsch et al., 2009). In this study, we use a single chunk of a "cubed sphere" mesh, with a width of ∼2,200 km, a height of ∼1,900 km, and a depth from the surface to the core, containing three doubling layers (Figure S2 in Supporting Information S1) to efficiently reduce computational effort (Lee et al., 2008).

The finite element mesh contains approximately 315,000 hexahedral elements, with Gauss-Lobatto-Legendre (GLL) interpolation grid node spacing of approximately 4.4 km at the surface, which provides accurate simulation for compressional waves with periods ≥8 s for velocities down to 5.1 km/s. The seismic parameters of P-wave velocity, S-wave velocity, and density are assigned to these GLL points. Figure S2 in Supporting Information S1 shows the mesh used for forward and adjoint simulations in this study. The mesh is unchanged throughout our iterative tomographic inversion.

3.2. Initial Model

An appropriate initial model is important for avoiding local minima and excessive iterations within a seismic tomographic inversion (Virieux & Operto, 2009). To make sure the tomographic results are as much as possible contributed by this new method, we start from a pseudo-3D initial model (Figure 4) rather than a 3D heterogeneous model (e.g., Berg et al., 2020; Gou et al., 2019; Nayak et al., 2020). We implement an undulating Moho discontinuity obtained from receiver function results (Zhang et al., 2019) in the Alaskan continent and from CRUST1.0 (Laske et al., 2013) in the adjacent oceanic region. Grid points in the mesh (GLL points) are then categorized as above or below the Moho, then assigned a velocity value according to our crustal or mantle model. The initial P-wave velocity of the GLL points in the crust is set according to the model of Eberhart-Phillips et al. (2006), which is a linear interpolation from 5.10 km/s on the surface to 7.15 km/s down to the lowermost crust. Similarly, for the GLL points located in the mantle (up to 300 km depth), we interpolate the velocity using

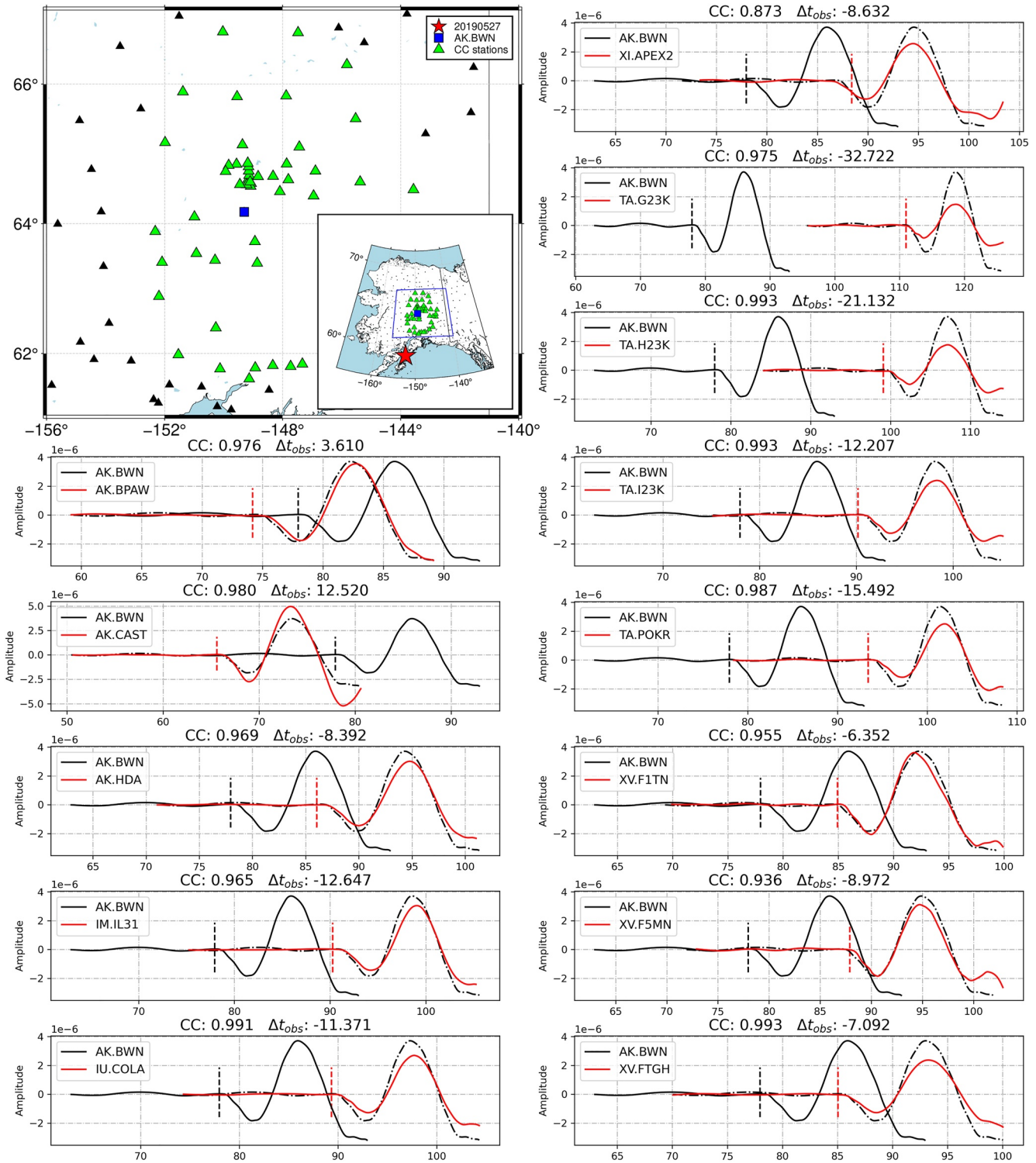

Figure 3. Example calculations of waveform cross-correlation. Upper left subfigure: distribution of seismic stations for one earthquake. The red star represents the earthquake. The reference station is denoted by the blue square. The green triangles are the stations that are cross-correlated with the reference station ("CC stations"). Other stations are plotted as black triangles. Subfigures for comparing waveforms: The vertical dashed lines mark the theoretical first P-wave arrival times. The black solid waveform is the processed signal recorded by the reference station. The red waveforms are processed signals recorded at the cross-correlated stations. The black dot-and-dash waveform shows the signal recorded by the reference station with a time shift (Δt_{obs}), where Δt_{obs} is the traveltime difference calculated via the cross-correlation technique. "CC" denotes the corresponding cross-correlation coefficient.

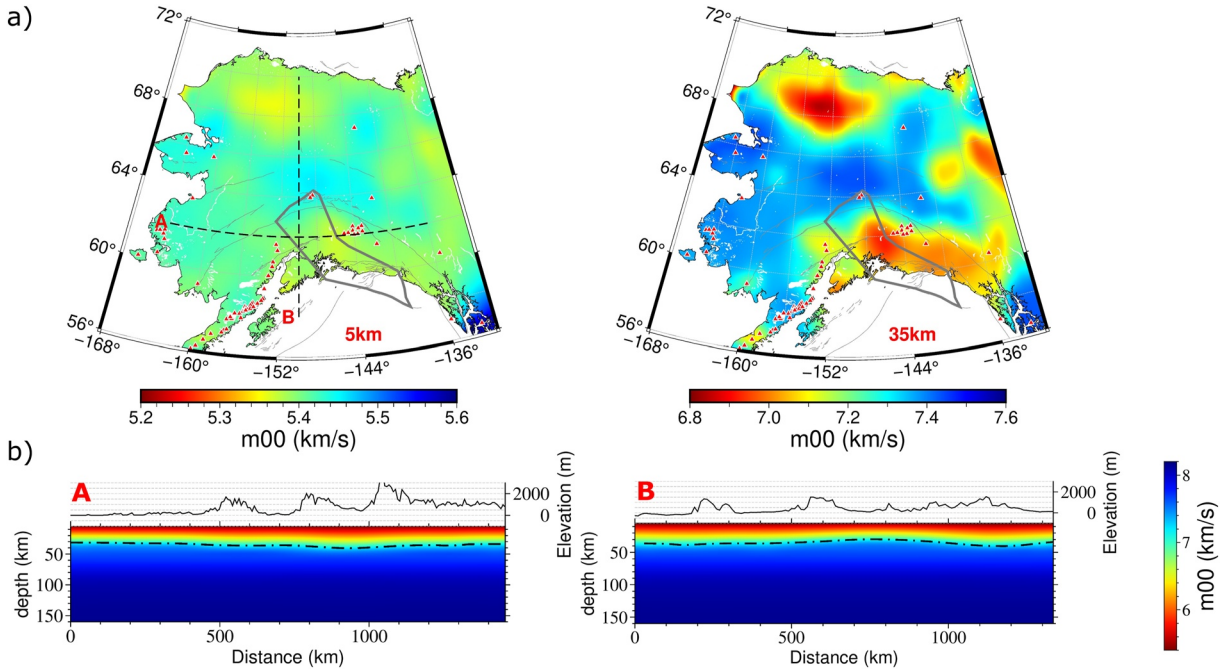

Figure 4. (a) Horizontal cross-sections of the initial 3D seismic velocity model m00. (b) Vertical cross-sections of m00, whose locations are plotted in the horizontal section as two orthogonal dashed lines a and b. The dot-and-dash line represents the Moho discontinuity used in this study, which is suggested by Zhang et al. (2019). Red mainly represents the crustal velocity in the initial model and blue mainly represents the mantle velocity. The horizontal sections can reflect the impact of the introduced Moho discontinuity on the initial velocity model.

a 1D layered model, which is generated by the lateral average of the AKAN2020 model (Nayak et al., 2020). Finally, the AK135 Vp model (Kennett et al., 1995) is adopted for the deeper domain to construct the initial model.

We compute double-difference measurements based on the initial model. Overall, 105,544 double-difference traveltimes are selected according to the aforementioned criteria. The mean value is near zero (0.019 s), indicating that the initial velocity model is not systematically too fast or too slow. On the other hand, the standard deviation (0.608 s) suggests the presence of significant differences between the initial model and the true model. For comparison, the 1D model AK135 produces double-difference measurements with a larger standard deviation (0.746) and fewer measurements (63,194) (Figure S3 in Supporting Information S1).

3.3. Inversion Method

We employ the adjoint waveform tomography method using common-source double-difference traveltime data to determine the P-wave velocity of the crust and uppermost mantle (Yuan et al., 2016). For the inversion, we parameterize the Vp perturbation on a coarser mesh with a size of $1° \times 0.5° \times 10$ km for the model update. This model parameterization has a smoothing effect on sensitivity kernels, which provides a form of regularization. The iterative inversion proceeds using a gradient descent method with a controlled step size (Tong, 2021). We set the upper and lower bounds of the Vp perturbation as $\pm 2\%$ in the beginning and then gradually reduce the bounds to $\pm 1\%$ by the fifth iteration. This approach of avoiding large-amplitude updates is similar to regularization.

4. Results

4.1. Checkerboard Resolution Test

We first perform a checkerboard resolution test to evaluate the resolving ability of the chosen seismic data (e.g., Humphreys & Clayton, 1988). First, the target model (t00) of the checkerboard test is constructed by assigning 8% alternating positive and negative Vp perturbations to the initial model (m00) used in the real data inversion. The size of the Vp anomaly block increases from $4° \times 2° \times 30$ km (longitude × latitude × depth) at the surface to

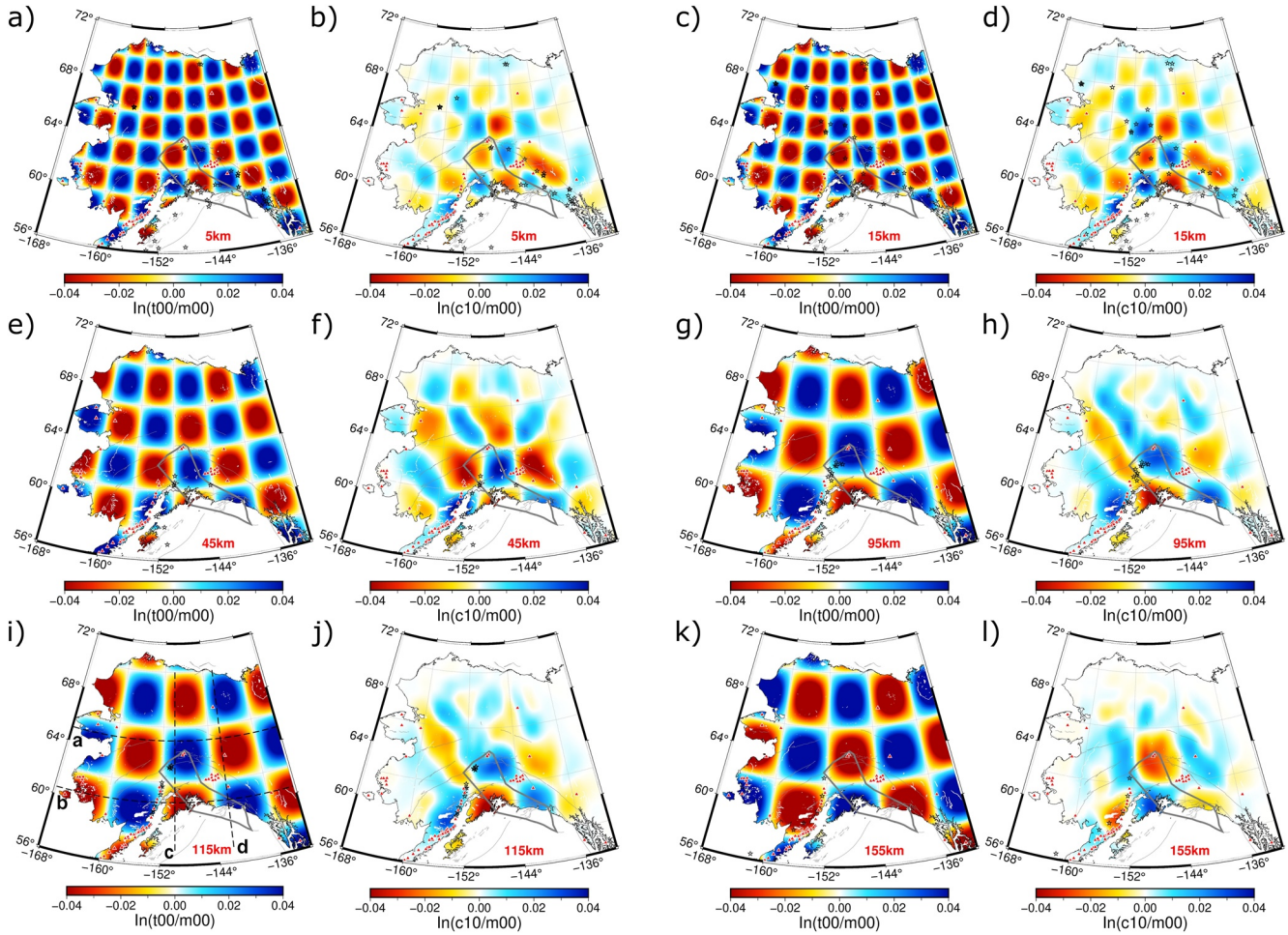

Figure 5. Horizontal cross-sections of the input checkerboard model (left: t00) and final output model (right: c10) at different depths. Both models are plotted with respect to the initial 3D velocity model m00. The anomaly blocks are outlined by faint gray dashed lines. The dashed lines in (i) denote the cross sections in Figure 6.

$8° \times 4° \times 50$ km in the upper mantle (Figures 5 and 6). Then, target waveforms for t00 are numerically computed via wavefield simulations. We then perform the same inversion procedure, but with target waveforms instead of real waveforms, to see how well the checkerboard model is recovered.

Ten iterations were carried out for the checkerboard resolution test, with the mean value of the squared double-difference traveltimes decreasing by ~87% (Figure S4 in Supporting Information S1). Vp perturbations of the target model (t00) and the inverted model (c10) relative to the initial model (m00) are aligned in horizontal and vertical sections in Figures 5 and 6 for comparison. Most checkerboard anomalies are recovered, suggesting that the double-difference traveltime data should be able to resolve comparable length scales of the true subsurface structure of mainland Alaska, especially in southern and central Alaska.

The results of the restoring resolution test are shown in Figures S5–S7 of Supporting Information S1, illustrating the reliability of the tomographic results. Thus, it is reasonable to believe that the labeled velocity anomalies in the real tomographic results are reliable features rather than artifacts.

4.2. Inversion Result Derived From Real Seismic Data

We perform 10 iterations, with each iteration requiring 147 simulations for synthetic seismograms and 147 adjoint simulations for sensitivity kernels. The mean value of the squared double-difference traveltimes decreases by approximately 55% (from 0.185 to 0.083 s^2). Figure 7a depicts the misfit reduction and the number of station pairs for each iteration. The value of the misfit function drops sharply in the first five iterations and then decreases

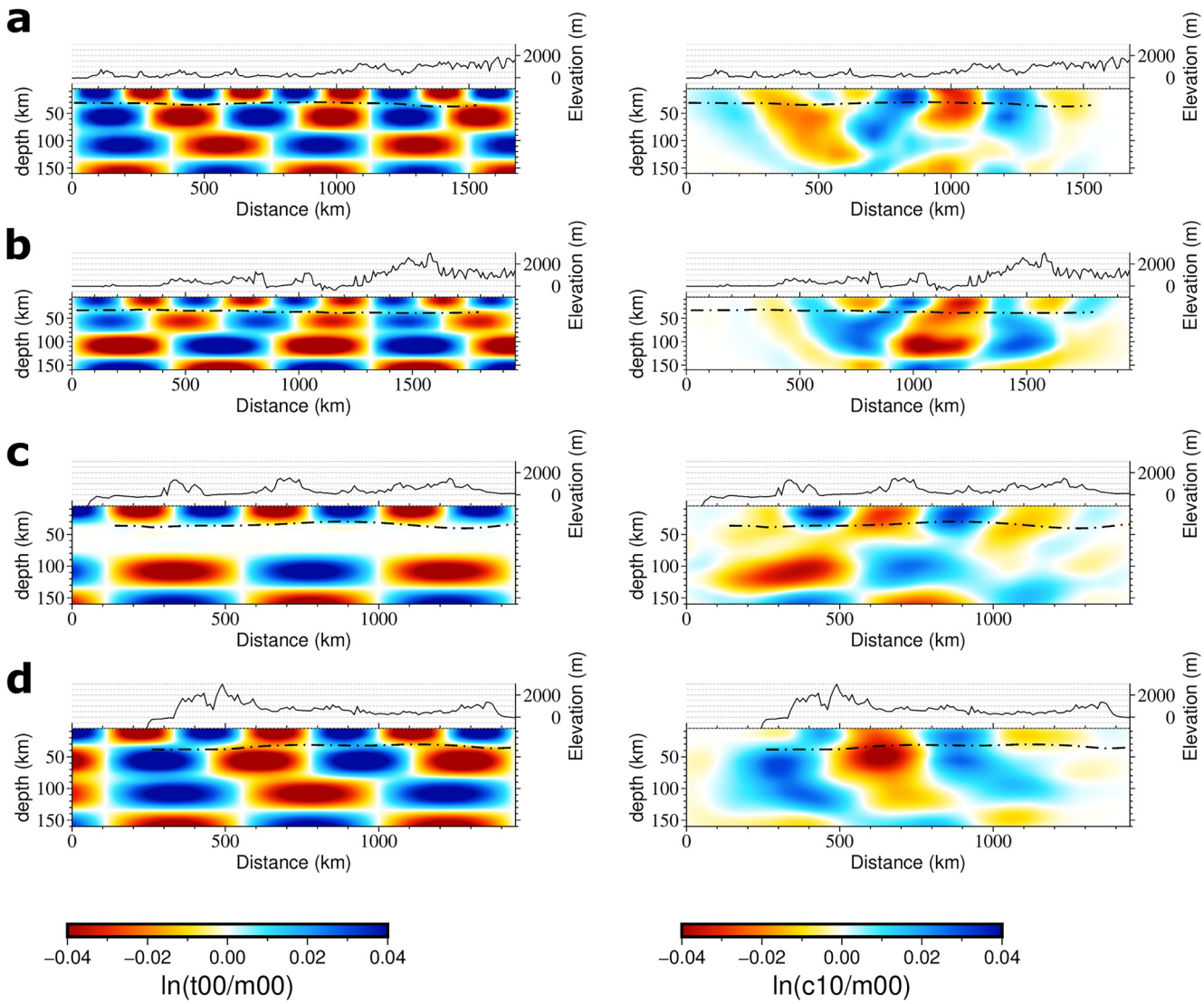

Figure 6. Vertical cross-sections of the input checkerboard model (left: t00) and final output model (right: c10). Both models are plotted with respect to the initial 3D velocity model m00. The locations of the cross-sections are plotted as black dashed lines a-d in Figure 5i. In detail, profiles a and b are located at latitudes 65° and 60.5°, respectively; and profiles c and d are located at longitudes −150° and −142°, respectively. The black dot-and-dash line denotes the Moho discontinuity.

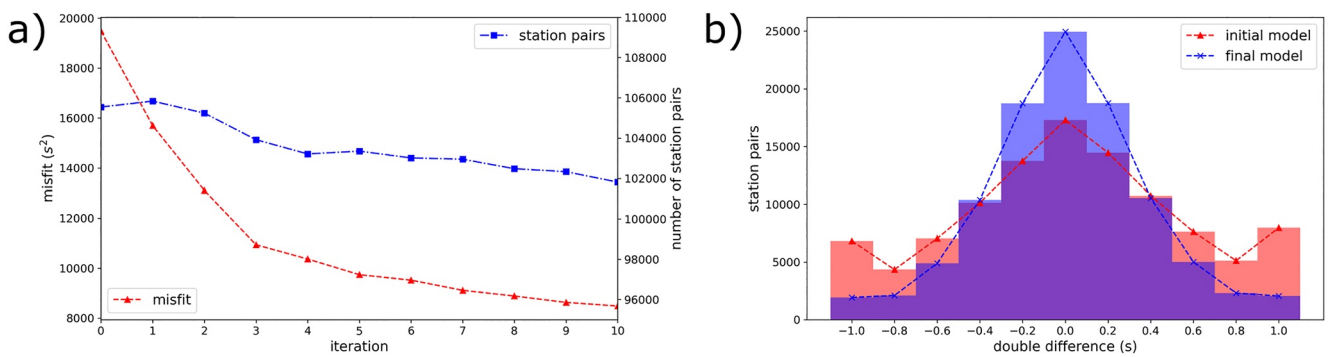

Figure 7. (a) The reduction of the misfit function (red) and the change of station pairs involved in the inversion through iteration (blue). (b) Comparison of double-difference traveltime measurements in the initial model (red: m00) and the final model (blue: m10). After the inversion (m00 to m10), the misfit function decreases by 56.5% (from 19,488 to 8,484 s^2). The standard variance (mean value) of the double-difference traveltimes is reduced from 0.607 to 0.408 s (0.019 to −0.0011 s).

gradually. On the other hand, the number of used station pairs decreases slightly, from 105,544 to 101,818. This decrease may arise from the reduction of cross-correlation coefficients: as iterations proceed, the modeled heterogeneity increases and generates more complex waveforms, which may lead to lower cross-correlation coefficients when aligning waveforms, causing some station pairs to be excluded. In addition, the double-difference traveltimes become more concentrated at zero (Figure 7b), with the standard deviation decreasing from 0.607 to 0.408 s.

Our inversion produces a 3-D P-wave velocity model down to a depth of 155 km. Similar to the checkerboard test, we use m00 to represent the initial 3D Vp model and m10 for the Vp model after the 10th iteration. We display the model in two ways: (a) m10 as Vp in km/s, (b) ln (m10/m00) as Vp perturbation. The first display is useful for geophysical and geological interpretations, while the second display conveys the changes made by the tomographic inversion. The first display includes any complexities present within the initial model, while the second display does not. In general, the two displays can look very different, especially in cases where the initial model contains strong, fine-scale heterogeneities. For all horizontal cross sections, the offshore areas are masked because of poor data coverage in the adjacent ocean.

Figure 8 contains horizontal sections of Vp and Vp perturbation, while Figure 9 contains vertical cross-sections of Vp perturbation. Figures S8–S13 in Supporting Information S1 provide additional comparisons of the initial model (m00) and final model (m10). In the shallow crust at 15 km depth, the imaged low-velocity anomalies in the absolute Vp model lie mainly beneath several large mountain ranges in Alaska. Specifically, significant low-velocity anomalies are revealed under the Brooks Range (L1), the Alaska Range (L2), and the Wrangell Mountains (L3). In the south, a high-velocity anomaly (H1) is detected under the Yakutat slab. In the cross section at 35 km depth, the distribution of Vp anomalies is related to the assumed Moho topography. The high-velocity anomaly H2 (Figures 8c and 8d) reflects a shallow Moho depth in central Alaska. It is in sharp contrast with the low-velocity anomalies in northern (L1 in Figures 8c and 8d) and southern Alaska (L2 and L3 in Figures 8c and 8d) where the crust is thicker. Furthermore, low-Vp anomalies are also observed beneath the Aleutian volcanic arc (L2) and the WVF (L3) in the Vp perturbation model, and L3 extends to the uppermost mantle down to 150 km depth. In the horizontal section at 65 km depth, a high-velocity anomaly (H3 in Figures 8e and 8f) is observed beneath the DVG and will be discussed later.

Spatial distributions of high- and low-velocity anomalies are similar in horizontal sections from 95 to 145 km depth. Prominent high-velocity anomalies are revealed in the northernmost (H4 in Figures 8g–8l and 9f) and northeastern (H5 in Figures 8g–8l, 9e, and 9f) parts of the study area. A high-velocity zone (H6 in Figures 8g–8l and 9a–9d) representing the subducting Pacific plate is clearly imaged from the Aleutian volcanic arc to the central Alaska region at ~65°. In the 125 km depth section, the strike of this anomaly dramatically changes at ~64°, forming a prominent kink (K1) and a bulge (A1) considerably exceeding north of the Wadati-Benioff zone. In addition, a relatively small high-velocity anomaly (H7 in Figures 8i, 8j, 9a, 9d, and 9e) is imaged in the south of the WVF. It is detached from the aforementioned high-velocity strip (H6) and disappears at greater depths, forming a distinct low-velocity zone near the WVF (L4 in Figures 8g–8j). Although the high-velocity anomalies A1 and H7 are smaller than the checkerboard test at corresponding depth (Figures 5i, 5j, 8i, and 8j), the restoring test (Figure S7 in Supporting Information S1) demonstrates that these anomalies are resolved.

5. Discussion

5.1. Pacific Plate Subduction

The subduction of the Pacific plate is a significant characteristic in Alaska, contributing to the distinct volcanism in southern Alaska and the Aleutian Islands. Our initial model (Section 3.2) is laterally varying but fairly simple and does not contain any subducting slab. From our inversion, we identify a substantial high-velocity anomaly (H6) in southern and central Alaska (Figures 8g–8l and 9a–9d), representing the subducting Pacific plate relative to the North America plate (Berg et al., 2020; Eberhart-Phillips et al., 2006; Feng & Ritzwoller, 2019; Gou et al., 2019; Jiang et al., 2018). This anomaly extends from the southern boundary of the study region to central Alaska at ~65° latitude, with its upper boundary consistent with Slab2.0 (Hayes et al., 2018) (Figures 9a–9d).

We discuss two characteristics of this subducting plate. The first one is the distinct kink at about (−152°, 64°) (Figures 8i–8l, K1), which illustrates the complex geometry of the subducting Pacific plate. This change of subduction is suggested to be associated with the development of a slab tear (Jiang et al., 2018). The segmentation

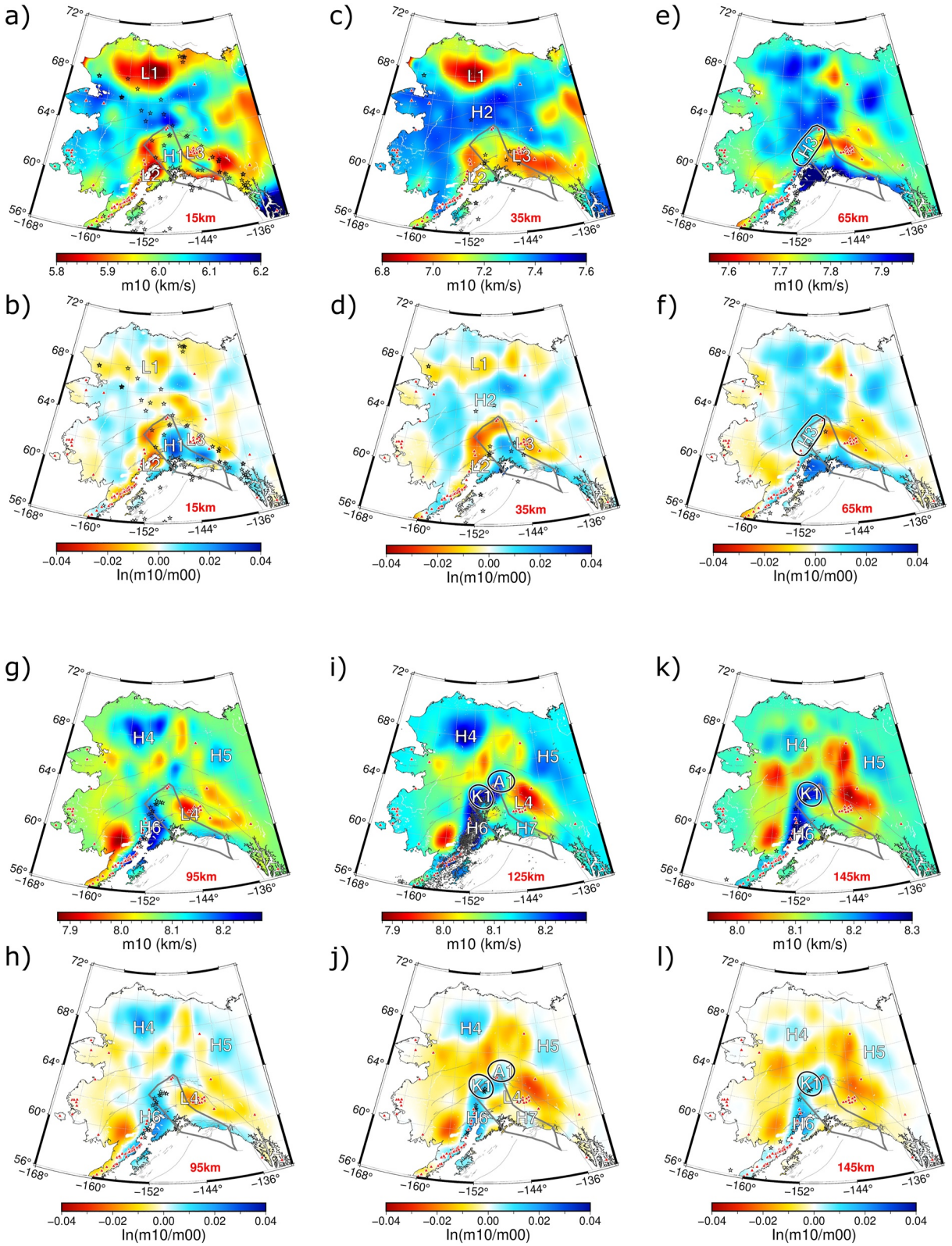

Figure 8.

of the subduction zone has also been observed in Ratchkovski and Hansen (2002) by investigating the seismicity of the Wadati–Benioff Zone. Second, a strong high-velocity anomaly is imaged at the eastern edge of the subducting plate (Figures 8i and 8j, A1), east of the Wadati-Benioff zone. This portion is interpreted as an aseismic slab edge, which may result from a shallower basalt-eclogite transition caused by the localized heating of the lithosphere near the slab edge (Martin-Short et al., 2018). This aseismic slab edge has also been imaged by many other studies (e.g., Feng & Ritzwoller, 2019; Gou et al., 2019; Jiang et al., 2018; Martin-Short et al., 2016; Wang & Tape, 2014).

5.2. Provenance of the Denali Volcanic Gap

A large-scale low-velocity anomaly (e.g., L2 in Figures 8c, 8d, and 9b–9d) is imaged beneath arc volcanoes in our results, which may reflect the arc magmatism associated with subduction of the Pacific plate. Tatsumi (1986) suggested that H_2O released from peridotite in the subducting slab could reform amphibole peridotites, lower the solidus temperature of peridotites, and generate initial magmas that rise as a mantle diapir. Interestingly, the L2 anomaly covers the Denali Volcanic Gap (DVG), a region marked by the absence of significant surface volcanism (McNamara & Pasyanos, 2002; Nayak et al., 2020; Rondenay et al., 2010). The DVG is identified as region H3 (Table 1) and plotted in Figures 8e and 8f.

McNamara and Pasyanos (2002) found a high Vp/Vs ratio zone under the DVG that was similar to the Vp/Vs ratio structures beneath adjacent arc volcanoes. Their result implies that melting materials are deposited in the mantle wedge under the DVG. Accordingly, they suggested that upwelling of mantle materials may be prevented by increased crustal compression near the northern apex of the curving Denali fault, resulting in the absence of volcanic activity in the DVG. In addition, attenuation imaging results and thermal modeling studies report high temperature (>1200°C) in the mantle wedge under the DVG (e.g., Rondenay et al., 2008; Stachnik et al., 2004). These results indicate the potential conditions for producing partial melting, supporting the hypothesis that the melting materials in the mantle wedge cannot reach the surface. By contrast, Rondenay et al. (2010) suggested that there is no melt accumulation in this area. They inferred that shallow subduction of the Yakutat slab cools the mantle wedge below the DVG and prevents the formation of a "pinch zone." This, in turn, reduces melt production and inhibits magma generation and extraction, resulting in the absence of surface volcanic activities. An alternative model, proposed by Chuang et al. (2017), suggests that dehydration of the shallow-angle subducting Yakutat slab only occurs at its upper crust, inhibiting the release of fluids and the generation of partial melts in the mantle wedge.

In the past decade, newly deployed seismic stations and the development of inversion techniques have enabled us to illuminate the subsurface structure at a higher resolution. The hypothesis proposed by Rondenay et al. (2010) has gained more support as high-velocity anomalies have been revealed beneath the DVG (e.g., Berg et al., 2020; Jiang et al., 2018; Nayak et al., 2020). Our model also images a high-velocity anomaly (H3) in the mantle wedge, indicating the absence of partial melting beneath the DVG (Yang & Gao, 2020), which could support the conjectures from Rondenay et al. (2010) or Chuang et al. (2017).

5.3. The Wrangell Volcanic Field

The Wrangell Volcanic Field (WVF) is situated on the northeastern margin of the subducted Yakutat slab. This group of volcanoes is dominated by calc-alkaline lavas, which are characteristic of continental volcanic arcs (Martin-Short et al., 2018). The WVF began at ∼26 Ma with a northwestward evolution of eruptive activity (Richter et al., 1990), which may be connected with the shallow-angle subduction of the Yakutat slab (Finzel et al., 2011). Given the weakness of seismicity (Stephens et al., 1984) below 40 km beneath the WVF (Figure 8j), the existence of a subducting plate under the WVF, as well as the origin of the WVF, is debatable (Berg et al., 2020; Daly et al., 2021; Gou et al., 2019; Jiang et al., 2018; Martin-Short et al., 2016).

One hypothesis suggests that the WVF is driven by a possibly existing slab, called the Wrangell slab. Its existence is supported by some deep earthquakes beneath the WVF (Daly et al., 2021; Stephens et al., 1984) and

Figure 8. Horizontal cross-sections of the inverted Vp model at different depths. (a, c, e, g, i, and k) The absolute P wave velocity m10. (b, d, f, h, j, and l) The Vp perturbation model ln (m10/m00) relative to the initial model m00. Prominent velocity anomalies are labeled (Table 1). Light gray lines denote active faults. The Yakutat slab is outlined by thick gray lines. Red triangles are active volcanoes. Black stars represent the earthquakes used in the inversion. Additional earthquakes with magnitude ≥3.0 and depth ≥40 km between 1 January 2000 and 31 August 2021 obtained from the ANSS ComCat (https://earthquake.usgs.gov/earthquakes/search) are plotted as smaller gray dots in (i) to illustrate the Wadati-Benioff seismicity.

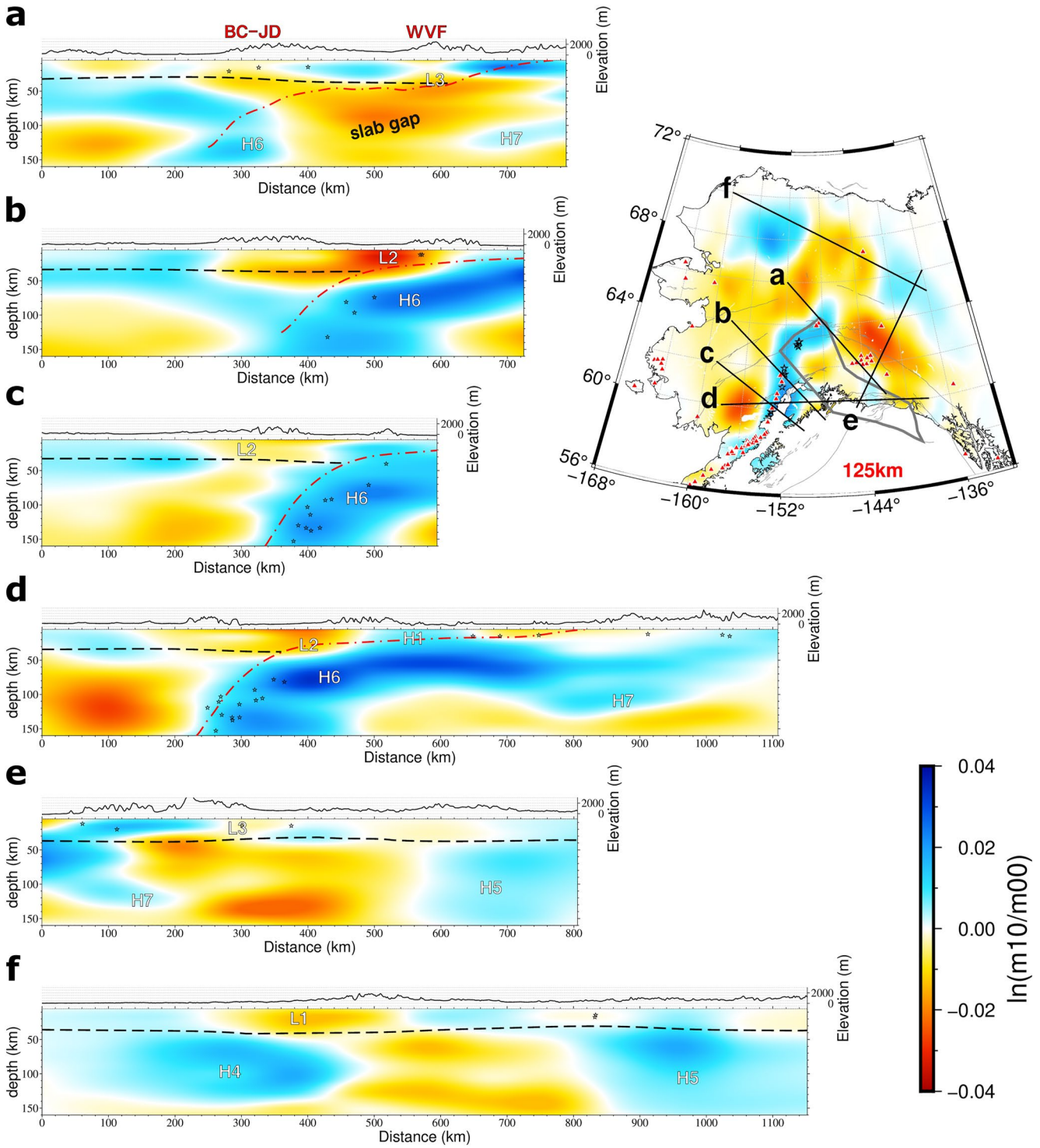

Figure 9. Vertical cross-sections of the Vp perturbation model ln (m10/m00). Prominent anomalies are labeled in each section (Table 1). The black dashed lines are the Moho discontinuity. The red dot-and-dash line represents the upper boundary of the Pacific subducting plate. The black stars in each cross-section indicate earthquakes that occurred from 1990 to 2020, with magnitude greater than 5.0, and within 30 km of the cross section.

further verified by several recent tomographic images (Gou et al., 2019; Jiang et al., 2018; Yang & Gao, 2020). Another hypothesis is that the WVF arises from slab edge mantle flow (Jadamec, 2016; Jadamec & Billen, 2010; Martin-Short et al., 2016; Venereau et al., 2019), which is supported by the presence of adakitic melts near the WVF (Brueseke et al., 2019; Preece & Hart, 2004). Some tomographic images also reveal a vertically continuous

Table 1
Tomographic Anomalies Labeled and Discussed in This Study

Label	Location	Depth (km)	Figures
L1	Brooks Range	5–50	Figures 8c, 8d, and 9f
L2	Arc volcanoes	5–50	Figures 8c, 8d, and 9b–9d
L3	Wrangell Volcanic Field	5–145	Figures 8c–8l, 9a, and 9e
L4	Slab gap	95–125	Figures 8g, 8i, 8h, and 8j
H1	Yakutat terrane	5–30	Figures 8a, 8b, and 9d
H2	Central Alaska	35	Figures 8c and 8d
H3	Denali Volcanic Gap	65	Figures 8e and 8f
H4	Northeast Alaska	40–145	Figures 8g–8l and 9f
H5	North American Craton	40–145	Figures 8g–8l, 9e, and 9f
H6	Subducting Pacific plate	95–145	Figures 8g–8l and 9a–9d
H7	Wrangell Volcanic Field	125	Figures 8i, 9a, 9d, and 9e
A1	Aseismic slab edge	125	Figures 8i and 8j
K1	Kink of the slab	125	Figures 8i and 8j

low-velocity anomaly beneath the WVF (Martin-Short et al., 2016; Ward, 2015), which is interpreted as mantle flow and in support of this hypothesis.

In our results, a spatially small high-Vp anomaly (H7) is observed near the WVF at a depth of 125 km (Figures 8i, 8j, 9a, 9d, and 9e), which is below (or within) the subducting Pacific/Yakutat plate. The detected high-velocity anomaly has a subtle location that is similar to the Wrangell slab imaged by Gou et al. (2019) but differs from the area (exactly beneath the WVF) imaged by Jiang et al. (2018), suggesting that H7 could represent the Wrangell slab. On the other hand, given that the majority of H7 in our tomographic results lies inside the outlines of the Yakutat slab, we still cannot rule out the possibility that H7 represents a high-velocity slab edge of the Yakutat slab (Berg et al., 2020; Martin-Short et al., 2018). Therefore, it is necessary to use higher-quality data set to explore the structure beneath the WVF in future works. In addition, our model shows a prominent gap (L4) of between the Pacific slab (H6) and high-velocity anomaly (H7) in the vicinity of the WVF (Figure 9a). Notably, the slab gap connects the WVF with the deeper mantle, which may provide a channel to transport mantle materials to surface volcanoes (Gou et al., 2019). The crustal low-velocity anomaly L3 (Figures 8c, 8d, and 9a) may represent widespread partial melting and high-temperature materials in the region of the slab gap.

6. Conclusions

We employ the adjoint waveform tomography method using common-source double-difference traveltime data to construct a 3-D P-wave velocity model of the crust and uppermost mantle in Alaska. A primary advantage of using double-difference traveltime data is that they are not sensitive to structure near the earthquake source nor to the earthquake source parameters themselves (i.e., source time function and origin time). By merging the double-difference technique with 3D seismic wavefield simulations, we are able to employ more accurate physics than traditional ray-based methods. Our results illustrate the potential of wave equation-based double-difference adjoint tomography methods for imaging subsurface structures. By performing checkerboard and restoring resolution tests that employ the same source-station coverage and 3D wavefield simulations as the real inversions, we provide a foundation for interpreting the results of our tomographic model.

Our model clearly reveals the Pacific plate subducting relative to the North America plate. Furthermore, a slab is detected at the eastern edge of the Pacific subducting plate, within a seismicity gap, suggesting the presence of an aseismic slab. Our tomographic model also contributes to a better understanding of the relationship between volcanism and subduction in Alaska. The first is the high-velocity zone revealed at a depth of 65 km under the DVG. It suggests a cold mantle wedge that could lead to a thickened lithosphere and prevent the formation of surface volcanoes. Second, the potential Wrangell slab (or the high-velocity slab edge of the Yakutat slab) is imaged as a high Vp anomaly near the WVF, which promotes volcanic accumulation in the WVF. Specifically, a slab gap is observed near WVF that could serve as a channel for the upward transit of hot mantle materials, feeding volcanoes on the surface. These imaging results enhance our understanding of the interaction between subducting plates and volcanoes.

Data Availability Statement

The seismic waveform data are available at the IRIS DMC (https://ds.iris.edu/ds/nodes/dmc/). The Alaska Earthquake Center (https://earthquake.alaska.edu/) and the National Earthquake Information Center of the United States Geological Survey (https://earthquake.usgs.gov/earthquakes/search/) provide high-quality arrival time data used in this study. These data can also be obtained using the Python library "libcomcat" (https://doi.org/10.5066/P91WN1UQ). Most figures are made with the Generic Mapping Tool (Wessel & Smith, 1991).

Acknowledgments
We thank Michael Bostock (Editor), Gregory Waite (Associate Editor), Arthur Rodgers, and Tianshi Liu for their constructive feedback and reviews. We thank Aibing Li for providing the Moho discontinuity model of Alaska. Our model named "Alaska_DD_Vp" is publicly available in https://doi.org/10.21979/N9/MQG8HN. Our study was supported by the National Natural Science Foundation of China (Grant 11871297), Tsinghua University Initiative Scientific Research Program and China Scholarship Council. JC and PT were also supported by the Minister of Education, Singapore, under its MOE AcRF Tier-2 Grant MOE2019-T2-2-112. CT was supported by U.S. National Science Foundation Grant EAR 1829447.

References

Baig, A. M., Dahlen, F. A., & Hung, S.-H. (2003). Traveltimes of waves in three-dimensional random media. *Geophysical Journal International*, *153*(2), 467–482. https://doi.org/10.1046/j.1365-246x.2003.01905.x

Benowitz, J. A., Layer, P. W., & Vanlaningham, S. (2014). Persistent long-term (*c*. 24 Ma) exhumation in the Eastern Alaska Range constrained by stacked thermochronology. In F. Jourdan, D. F. Mark, & C. Verati (Eds.), *Advances in $^{40}Ar/^{39}Ar$ dating: From Archaeology to Planetary Sciences* (Vol. 378). Geological Society. https://doi.org/10.1144/SP378.12

Berg, E. M., Lin, F.-C., Allam, A., Schulte-Pelkum, V., Ward, K. M., & Shen, W. (2020). Shear velocity model of Alaska via joint inversion of Rayleigh wave ellipticity, phase velocities, and receiver functions across the Alaska Transportable Array. *Journal of Geophysical Research: Solid Earth*, *125*(2), e2019JB018582. https://doi.org/10.1029/2019JB018582

Brueseke, M. E., Benowitz, J. A., Trop, J. M., Davis, K. N., Berkelhammer, S. E., Layer, P. W., & Morter, B. K. (2019). The Alaska Wrangell arc: ~30 Ma of subduction-related magmatism along a still active arc-transform junction. *Terra Nova*, *31*(1), 59–66. https://doi.org/10.1111/ter.12369

Busby, R. W., & Aderhold, K. (2020). The Alaska transportable array: As built. *Seismological Research Letters*, *91*(6), 3017–3027. https://doi.org/10.1785/0220200154

Cameron, C. (2004). The geologic database of information on volcanoes in Alaska (GeoDIVA): A comprehensive and authoritative source for volcanic information. *Alaska GeoSurvey News*, *7*(1), 1–2.

Chen, J., Chen, G., Wu, H., Yao, J., & Tong, P. (2022). Adjoint tomography of northeast Japan revealed by common-source double-difference travel-time data. *Seismological Research Letters*, *93*(3), 1835–1851. https://doi.org/10.1785/0220210317

Christeson, G. L., Gulick, S. P. S., van Avendonk, H. J. A., Worthington, L. L., Reece, R. S., & Pavlis, T. L. (2010). The Yakutat terrane: Dramatic change in crustal thickness across the Transition fault, Alaska. *Geology*, *38*(10), 895–898. https://doi.org/10.1130/g31170.1

Chuang, L., Bostock, M., Wech, A., & Plourde, A. (2017). Plateau subduction, intraslab seismicity, and the Denali (Alaska) volcanic gap. *Geology*, *45*(7), 647–650. https://doi.org/10.1130/G38867.1

Colpron, M., Nelson, J. L., & Murphy, D. C. (2007). Northern Cordilleran terranes and their interactions through time. *Geological Society of America Today*, *17*(4/5), 4–10. https://doi.org/10.1130/GSAT01704-5A.1

Crotwell, H. P., Owens, T. J., & Ritsema, J. (1999). The TauP Toolkit: Flexible seismic travel-time and ray-path utilities. *Seismological Research Letters*, *70*(2), 154–160. https://doi.org/10.1785/gssrl.70.2.154

Dahlen, F. A., Hung, S.-H., & Nolet, G. (2000). Fréchet kernels for finite-frequency traveltimes—I. *Theory. Geophysical Journal International*, *141*(1), 157–174. https://doi.org/10.1046/j.1365-246x.2000.00070.x

Daly, K. A., Abers, G. A., Mann, M. E., Roecker, S., & Christensen, D. H. (2021). Subduction of an oceanic plateau across southcentral Alaska: High-resolution seismicity. *Journal of Geophysical Research: Solid Earth*, *126*(11), e2021JB022809. https://doi.org/10.1029/2021JB022809

DeMets, C., Gordon, R. G., Argus, D. F., & Stein, S. (1994). Effect of recent revisions to the geomagnetic reversal time scale on estimates of current plate motions. *Geophysical Research Letters*, *21*(20), 2191–2194. https://doi.org/10.1029/94gl02118

Eberhart-Phillips, D., Christensen, D. H., Brocher, T. M., Hansen, R., Ruppert, N. A., Haeussler, P. J., & Abers, G. A. (2006). Imaging the transition from Aleutian subduction to Yakutat collision in central Alaska, with local earthquakes and active source data. *Journal of Geophysical Research*, *111*(B11), B11303. https://doi.org/10.1029/2005JB004240

Feng, L., & Ritzwoller, M. H. (2019). A 3-D shear velocity model of the crust and uppermost mantle beneath Alaska including apparent radial anisotropy. *Journal of Geophysical Research: Solid Earth*, *124*(10), 10468–10497. https://doi.org/10.1029/2019JB018122

Ferris, A., Abers, G. A., Christensen, D. H., & Veenstra, E. (2003). High resolution image of the subducted Pacific (?) plate beneath central Alaska, 50–150 km depth. *Earth and Planetary Science Letters*, *214*(3–4), 575–588. https://doi.org/10.1016/s0012-821x(03)00403-5

Finzel, E. S., Trop, J. M., Ridgway, K. D., & Enkelman, E. (2011). Upper plate proxies for flat-slab subduction processes in southern Alaska. *Earth and Planetary Science Letters*, *303*(3–4), 348–360. https://doi.org/10.1016/j.epsl.2011.01.014

Gou, T., Zhao, D., Huang, Z., & Wang, L. (2019). Aseismic deep slab and mantle flow beneath Alaska: Insight from anisotropic tomography. *Journal of Geophysical Research: Solid Earth*, *124*(2), 1700–1724. https://doi.org/10.1029/2018JB016639

Hayes, G. P., Moore, G. L., Portner, D. E., Hearne, M., Flamme, H., Furtney, M., & Smoczyk, G. M. (2018). Slab2, a comprehensive subduction zone geometry model. *Science*, *362*(6410), 58–61. https://doi.org/10.1126/science.aat4723

Humphreys, E., & Clayton, R. W. (1988). Adaptation of back projection tomography to seismic travel time problems. *Journal of Geophysical Research*, *93*(B2), 1073–1085. https://doi.org/10.1029/jb093ib02p01073

Hung, S.-H., Dahlen, F. A., & Nolet, G. (2001). Wavefront healing: A banana-doughnut perspective. *Geophysical Journal International*, *146*(2), 289–312. https://doi.org/10.1046/j.1365-246x.2001.01466.x

Jadamec, M. A. (2016). Insights on slab-driven mantle flow from advances in three-dimensional modelling. *Journal of Geodynamics*, *100*, 51–70. https://doi.org/10.1016/j.jog.2016.07.004

Jadamec, M. A., & Billen, M. I. (2010). Reconciling surface plate motions with rapid three-dimensional mantle flow around a slab edge. *Nature*, *465*(7296), 338–341. https://doi.org/10.1038/nature09053

Jiang, C., Schmandt, B., Ward, K. M., Lin, F.-C., & Worthington, L. L. (2018). Upper mantle seismic structure of Alaska from Rayleigh and *S* wave tomography. *Geophysical Research Letters*, *45*(19), 10350–10359. https://doi.org/10.1029/2018GL079406

Kennett, B. L. N., Engdahl, E. R., & Buland, R. (1995). Constraints on seismic velocities in the Earth from traveltimes. *Geophysical Journal International*, *122*(1), 108–124. https://doi.org/10.1111/j.1365-246x.1995.tb03540.x

Kissling, E., & Lahr, J. C. (1991). Tomographic image of the Pacific slab under southern Alaska. *Eclogae Geologicae Helvetiae*, *84*(2), 297–315.

Komatitsch, D. (2011). Fluid–solid coupling on a cluster of GPU graphics cards for seismic wave propagation. *Comptes Rendus Mecanique*, *339*(2–3), 125–135. https://doi.org/10.1016/j.crme.2010.11.007

Komatitsch, D., Michéa, D., & Erlebacher, G. (2009). Porting a high-order finite-element earthquake modeling application to NVIDIA graphics cards using CUDA. *Journal of Parallel and Distributed Computing*, *69*(5), 451–460. https://doi.org/10.1016/j.jpdc.2009.01.006

Komatitsch, D., & Tromp, J. (2002a). Spectral-element simulations of global seismic wave propagation—I. Validation. *Geophysical Journal International*, *149*(2), 390–412. https://doi.org/10.1046/j.1365-246x.2002.01653.x

Komatitsch, D., & Tromp, J. (2002b). Spectral-element simulations of global seismic wave propagation—II. Three-dimensional models, oceans, rotation and self-gravitation. *Geophysical Journal International*, *150*(1), 308–318. https://doi.org/10.1046/j.1365-246x.2002.01716.x

Komatitsch, D., & Vilotte, J.-P. (1998). The spectral element method: An efficient tool to simulate the seismic response of 2D and 3D geological structures. *Bulletin of the Seismological Society of America*, *88*(2), 368–392. https://doi.org/10.1785/bssa0880020368

Laske, G., Masters, G., Ma, Z., & Pasyanos, M. E. (2013). Update on CRUST1.0: A 1-degree global model of Earth's crust. In *Geophysical Research Abstracts* (Vol. 15). Abstract EGU2013-2658.

Lee, S.-J., Chen, H.-W., Liu, Q., Komatitsch, D., Huang, B.-S., & Tromp, J. (2008). Three-dimensional simulations of seismic-wave propagation in the Taipei basin with realistic topography based upon the spectral-element method. *Bulletin of the Seismological Society of America*, *98*(1), 253–264. https://doi.org/10.1785/0120070033

Liu, Q., & Tromp, J. (2006). Finite-frequency kernels based on adjoint methods. *Bulletin of the Seismological Society of America*, *96*(6), 2383–2397. https://doi.org/10.1785/0120060041

Liu, Q., & Tromp, J. (2008). Finite-frequency sensitivity kernels for global seismic wave propagation based upon adjoint methods. *Geophysical Journal International*, *174*(1), 265–286. https://doi.org/10.1111/j.1365-246x.2008.03798.x

Mann, M. E., Abers, G. A., Daly, K. A., & Christensen, D. H. (2022). Subduction of an oceanic plateau across southcentral Alaska: Scattered-wave imaging. *Journal of Geophysical Research: Solid Earth*, *127*(1), e2021JB022697. https://doi.org/10.1029/2021JB022697

Martin-Short, R., Allen, R., Marstow, I. D., Porritt, R. W., & Miller, M. S. (2018). Seismic imaging of the Alaska subduction zone: Implications for slab geometry and volcanism. *Geochemistry, Geophysics, Geosystems*, *19*(11), 4541–4560. https://doi.org/10.1029/2018GC007962

Martin-Short, R., Allen, R. M., & Barstow, I. D. (2016). Subduction geometry beneath south central Alaska and its relationship to volcanism. *Geophysical Research Letters*, *43*(18), 9509–9517. https://doi.org/10.1002/2016GL070580

McNamara, D. E., & Pasyanos, M. E. (2002). Seismological evidence for a sub-volcanic arc mantle wedge beneath the Denali volcanic gap, Alaska. *Geophysical Research Letters*, *29*(16), 61-1–61-4. https://doi.org/10.1029/2001GL014088

Miller, M. S., & Moresi, L. (2018). Mapping the Alaska Moho. *Seismological Research Letters*, *89*(6), 2430–2436. https://doi.org/10.1785/0220180222

Nayak, A., Eberhart-Phillips, D., Ruppert, N., Fang, H., Moore, M. M., Tape, C., et al. (2020). 3D seismic velocity models for Alaska from joint tomographic inversion of body-wave and surface-wave data. *Seismological Research Letters*, *91*(6), 3106–3119. https://doi.org/10.1785/0220200214

Peter, D., Komatitsch, D., Luo, Y., Martin, R., Le Goff, N., Casarotti, E., et al. (2011). Forward and adjoint simulations of seismic wave propagation on fully unstructured hexahedral meshes. *Geophysical Journal International*, *186*(2), 721–739. https://doi.org/10.1111/j.1365-246x.2011.05044.x

Plafker, G., & Berg, H. C. (1994). Overview of the geology and tectonic evolution of Alaska. In G. Plafker & H. C. Berg (Eds.), *Geology of Alaska* (Vol. G-1, pp. 989–1021). Geological Society of America.

Pratt, R. G. (1999). Seismic waveform inversion in the frequency domain, Part 1: Theory and verification in a physical scale model. *Geophysics*, *64*(3), 888–901. https://doi.org/10.1190/1.1444597

Preece, S. J., & Hart, W. K. (2004). Geochemical variations in the <5 Ma Wrangell volcanic field, Alaska: Implications for the magmatic and tectonic development of a complex continental arc system. *Tectonophysics*, *392*(1–4), 165–191. https://doi.org/10.1016/j.tecto.2004.04.011

Qi, C., Zhao, D., & Chen, Y. (2007). Search for deep slab segments under Alaska. *Physics of the Earth and Planetary Interiors*, *165*(1–2), 68–82. https://doi.org/10.1016/j.pepi.2007.08.004

Ratchkovski, N. A., & Hansen, R. A. (2002). New evidence for segmentation of the Alaska subduction zone. *Bulletin of the Seismological Society of America*, *92*(5), 1754–1765. https://doi.org/10.1785/0120000269

Richter, D. H., Smith, J. G., Lanphere, M. A., Dalrymple, G. B., Reed, B. L., & Shew, N. (1990). Age and progression of volcanism, Wrangell volcanic field, Alaska. *Bulletin of Volcanology*, *53*(1), 29–44. https://doi.org/10.1007/bf00680318

Rondenay, S., Abers, G. A., & van Keken, P. E. (2008). Seismic imaging of subduction zone metamorphism. *Geology*, *36*(4), 275–278. https://doi.org/10.1130/g24112a.1

Rondenay, S., Montési, L. G. J., & Abers, G. A. (2010). New geophysical insight into the origin of the Denali volcanic gap. *Geophysical Journal International*, *182*(2), 613–630. https://doi.org/10.1111/j.1365-246x.2010.04659.x

Stachnik, J. C., Abers, G. A., & Christensen, D. H. (2004). Seismic attenuation and mantle wedge temperatures in the Alaska subduction zone. *Journal of Geophysical Research*, *109*(B10), B10304. https://doi.org/10.1029/2004JB003018

Stephens, C. D., Fogelman, K. A., Lahr, J. C., & Page, R. A. (1984). Wrangell Benioff zone, southern Alaska. *Geology*, *12*(6), 373–376. https://doi.org/10.1130/0091-7613(1984)12<373:wbzsa>2.0.co;2

Tatsumi, Y. (1986). Formation of the volcanic front in subduction zones. *Geophysical Research Letters*, *13*(8), 717–720. https://doi.org/10.1029/GL013i008p00717

Tian, Y., & Zhao, D. (2012). Seismic anisotropy and heterogeneity in the Alaska subduction zone. *Geophysical Journal International*, *190*(1), 629–649. https://doi.org/10.1111/j.1365-246X.2012.05512.x

Tong, P. (2021). Adjoint-state traveltime tomography: Eikonal equation-based methods and application to the Anza area in southern California. *Journal of Geophysical Research: Solid Earth*, *126*(5), e2021JB021818. https://doi.org/10.1029/2021JB021818

Venereau, C. M. A., Martin-Short, R., Bastow, I. D., Allen, R. M., & Kounoudis, R. (2019). The role of variable slab dip in driving mantle flow at the eastern edge of the Alaskan subduction margin: Insights from SKS shear-wave splitting. *Geochemistry, Geophysics, Geosystems*, *20*, 2433–2448. https://doi.org/10.1029/2018GC008170

Virieux, J., & Operto, S. (2009). An overview of full-waveform inversion in exploration geophysics. *Geophysics*, *74*(6), WCC1–WCC26. https://doi.org/10.1190/1.3238367

Wang, Y., & Tape, C. (2014). Seismic velocity structure and anisotropy of the Alaska subduction zone derived from surface wave tomography. *Journal of Geophysical Research: Solid Earth*, *119*(12), 8845–8865. https://doi.org/10.1002/2014JB011438

Ward, K. M. (2015). Ambient noise tomography across the southern Alaskan Cordillera. *Geophysical Research Letters*, *42*(9), 3218–3227. https://doi.org/10.1002/2015GL063613

Ward, K. M., & Lin, F.-C. (2018). Lithospheric structure across the Alaskan cordillera from the joint inversion of surface waves and receiver functions. *Journal of Geophysical Research: Solid Earth*, *123*(10), 8780–8797. https://doi.org/10.1029/2018JB015967

Wessel, P., & Smith, W. H. F. (1991). Free software helps map and display data. *Eos, Transactions American Geophysical Union*, *72*(41), 441–446. https://doi.org/10.1029/90eo00319

Woodward, M. J. (1992). Wave-equation tomography. *Geophysics*, *57*(1), 15–26. https://doi.org/10.1190/1.1443179

Yang, X., & Gao, H. (2020). Segmentation of the Aleutian-Alaska subduction zone revealed by full-wave ambient noise tomography: Implications for the along-strike variation of volcanism. *Journal of Geophysical Research: Solid Earth*, *125*(11), 1–20. https://doi.org/10.1029/2020JB019677

Yuan, Y. O., Simons, F. J., & Tromp, J. (2016). Double-difference adjoint seismic tomography. *Geophysical Journal International*, *206*(3), 1599–1618. https://doi.org/10.1093/gji/ggw233

Zhang, Y., Li, A., & Hu, H. (2019). Crustal structure in Alaska from receiver functions. *Geophysical Research Letters*, *46*(3), 1284–1292. https://doi.org/10.1029/2018GL081011

Zhao, D., Christensen, D., & Pulpan, H. (1995). Tomographic imaging of the Alaska subduction zone. *Journal of Geophysical Research*, *100*(B4), 6487–6504. https://doi.org/10.1029/95jb00046